Settling dynamics of Brownian chains in viscous fluids

Lucas H. P. Cunha, 1,2,* Jingjing Zhao, 1,*
Fred C. MacKintosh, 1,3,2,4,† and Sibani Lisa Biswal

¹Department of Chemical and Biomolecular Engineering, Rice University, Houston, Texas 77005, USA ²Center for Theoretical Biological Physics, Rice University, Houston, Texas 77005, USA ³Department of Physics and Astronomy, Rice University, Houston, Texas 77005, USA ⁴Department of Chemistry, Rice University, Houston, Texas 77005, USA



(Received 11 May 2021; accepted 11 March 2022; published 30 March 2022)

We investigate the dynamics of sedimenting Brownian filaments using experimental, computational, and theoretical approaches. The filaments under consideration are composed of linked colloidal particles that form bead-spring-like chains. Under the action of gravitational forces, the nonlocal hydrodynamic interactions cause the filaments to bend and rotate to get their end-to-end direction perpendicular to gravity. Different reorientation mechanisms are verified for different regimes of flexibility, characterized by the elastogravitational number. The thermal forces promote shape and orientation fluctuations around the steady configurations of the reciprocal non-Brownian chains. The competition between the reorientation mechanisms and the Brownian effects results in normal distributions of the orientation of the chains. In the stiff regime, these fluctuations cause the chains to fall faster than their reciprocal non-Brownian cases. With increasing flexibility, thermal fluctuations lead to more compact configurations of the chains and higher average settling velocity. Nonetheless, chain flexibility plays an important role on lateral migration. The interplay between elastic, gravitational, and thermal forces leads to important secondary influences on the filament settling dynamics.

DOI: 10.1103/PhysRevFluids.7.034303

I. INTRODUCTION

The sedimentation of elastic filaments is a problem of great interest in the fields of biological systems and the fabrication of complex materials. The coupling between elastic and hydrodynamic effects induce complex dynamics of deformation and reorientation, impacting in the micro and macrotransport phenomena [1]. As pioneers in the subject, Xu and Nadin [2] were the first to attack the problem from a theoretical point of view. They described an analytical solution for the regime of small deformation amplitudes using the slender body model together with the Euler-Bernoulli beam theory. Their model predicted the mechanism of reorientation, in which the elastic filaments rotate to get perpendicularly oriented with the driven force of gravity. Approximately ten years later (2005), Lagomarsino et al. [3] and Schlagberger and Netz [4] conducted numerical investigations on the sedimentation of the single elastic filaments problem using the bead-spring model. Due to the applied numerical techniques, both works were able to explore regimes of larger amplitude deflections compared to Xu and Nadin. In fact, Lagomarsino et al. identified a marginally stable W-like shape configuration for highly flexible chains. From conducting numerical simulations, but

^{*}These authors contributed equally to this work.

[†]Corresponding authors: fcmack@rice.edu; biswal@rice.edu

using the slender body theory, Li *et al.* [5] observed that in the highly flexible regime the filaments are susceptible to a buckling instability when sedimenting along its long axis.

Later works came up with investigations on the dynamics of interacting particles and filaments in Stokes' regimes. Jung et al. [6] described tumbling orbits dynamics for pairs of identical rigid particles sedimenting in the Stokes' regime from both experiments and numerical simulations. The particles mutually induce an in-phase rotational motion together with periodic modulations of separation distance. Similar mechanisms were observed by Bukowicki and Ekiel-Jezewska [7] for the sedimentation of interacting elastic trumbbells, Llopis and Pagonabarraga [8] described the interactions between inextensible semi-flexible filaments. From numerical simulations using the bead-spring model, they concluded that the sedimentation of a pair of semi-flexible filaments is qualitatively different from that of rigid rods. For initially parallel coplanar filaments, the top one presents a larger deformation and sediments faster, leading to pair collision (an effect also observed by Saggiorato et al. [9]). The authors identified other rich behaviors, such as periodic trajectories, unsteady conformations, and filament rotations due to asymmetric initial conditions. Buckowicki and Ekiel-Jezewska [10] extended investigations in this matter by considering a large family of initial pair of filaments configurations. Using large-scale numerical simulations, Gustavsson and Tornberg [11] studied the complex sedimentation dynamics of a cluster of rigid fibers. They considered up to 800 fibers through their simulations. Investigating the average fibers orientation and the fluctuations in the sedimentation velocity, they observed that the dynamical behavior of the system is very sensitive to small random differences in the initial configuration. Recently, Marchetti et al. [12] presented experimental results for a single non-Brownian filament sedimenting a viscous fluid. The authors observed good agreement with numerical predictions for both the slender body and the bead-spring models. The limited flexibility of the experimental filaments prevented the observation of W-like shapes predicted by numerical simulations.

Recent works explored the development of sophisticated techniques that made it possible for the synthesis of sophisticated colloidal structures to mimic diverse types of molecular systems [13–19]. Colloidal model systems have shown to be of great value to study the behavior of polymers and fibers in the more diverse conditions [20,21]. The particles are large enough to be observed with optical microscopy, however, small enough so that their dynamics are influenced by thermal motion. By tracking the chain position and shape in time, we can obtain a precise description of its dynamics. In practice, the colloidal chains experimentally mimic the classic mathematical bead-spring model used for polymers and fibers [22–24]. Also, the tunable elasticity and contour length make it possible to investigate a vast range of physical regimes. The complex dynamics of such chains when subjected to external flows and body forces is given by the interplay between the particles' hydrodynamics interactions, internal elastic forces, and stochasticity of thermal fluctuations.

In this work, we investigate the settling dynamics of Brownian colloidal chains in a viscous fluid using microscopical experiments and numerical simulations. The experimental chains are fabricated by connecting micron-sized beads with DNA [19,21,25,26]. The multiple chain lengths permits us to explore in a singe experiment a wide range of ratios between gravitational to elastic forces, characterized by the elastogravitational number β . Conveniently, we use the classical bead-spring model to perform numerical investigations. This methodology allows us to better understand the mechanisms of reorientation observed for the settling flexible filaments, as well as the dynamic that leads the filaments to the meta-stable W-like configuration recurrently verified in the literature. Moreover, we account for Brownian motion effects to statistically study its implications on the chain settling dynamics. The numerical approach allows us to provide investigations considering wide ranges of parameters associated with the chains' flexibility and thermal fluctuations. From scale analysis, we describe the orientation distribution of the chains overtime for the rigid limit, elucidating the increase in the settling velocity caused by the Brownian motions.

II. EXPERIMENTAL VISUALIZATION

A. Colloidal chains preparation

The Brownian colloidal filaments used in these experiments were synthesized using a directed assembly method with double-stranded DNA (dsDNA) linkers. The particles used in the experiments are streptavidin-coated superparamagnetic polystyrene spheres (Dynabeads MyOne Streptavidin C1, Thermo Fisher Scientific Inc.). The particle diameter is $2a = 1.05 \pm 0.1 \,\mu\text{m}$. The particle density $\rho_p = 1.8 \,\text{g/cm}^3$. The linkers used are 4000 base pair dsDNA that are biotinylated on the 5' ends. A solution of 0.01 wt% of particles, 5 nM of dsDNA linkers and 10 mM phosphate buffer solution (PBS) (pH 7.4) were mixed and placed in a horizontal chamber with an approximate size $2 \,\text{cm} \times 2 \,\text{cm} \times 80 \,\mu\text{m}$. On applying a constant external magnetic field, the superparamagnetic particles align into linear chain-like structures. The biotinylated dsDNA linkers crosslink neighboring particles by forming biotin-streptavidin bonds. Filament properties such as length and flexibility can be tuned by modifying the time under the external magnetic field, the strength of the external field, and the temperature of the filament linking system. The filaments synthesized have a persistence length to contour length ratio (L_p/L) that varied from approximately 5 to 17. A detailed description of filament fabrication and control of chain rigidity was reported by Byrom *et al.* [21].

B. Experimental setup and data acquisition

To visualize the gravity-driven settling dynamics of the colloidal filaments, we placed the glass chamber containing the chains samples on an inverted microscope with a 85° tilt angle from horizontal. The chains dynamics were first observed using a 40X/0.95 (air) Olympus objective. The filaments stay within the focal plane for the entire experimental recording. The density of the particles and and the inclination of the system, along with electrostatic repulsive interactions with the wall, induce *quasi*-two-dimensional (2-D) dynamics of the chains while settling.

To record and analyze the sedimentation dynamics, a charge coupled device (CCD) camera (Orca-HR from Hamamatsu Inc., Sewickley, PA) was attached to the microscope with a 10X/0.30 (air) or a 40X/0.60 (air) Olympus objective. Images of the filaments were captured at a rate of 10 frames/s using HCIMAGE, an image acquisition software from Hamamatsu Corporation (Bridgewater, NJ). A snapshot taken from the experiment is presented in Fig. 1(a) as a matter of illustration. The contours of filaments are tracked using JFILAMENT plugin [27,28] in Fiji, an open-source NIH software [29], which searches for the darkest ridges at the central line of each filament based on stretching and deforming open active contours, as presented in Fig. 1(b). Lastly, the gyration tensor was calculated from the images to compute geometrical parameters of the chains, as shown by the schematic in Fig. 1(c). The gyration tensor is calculated as $G_{nm} = 1/L \int_0^L [(r_n(s,t) - \bar{r}_n(t)][r_m(s,t) - \bar{r}_m(t)]ds$, where r is the position along the filament, \bar{r} is the center of mass of the chain under analysis, and t is time.

C. Experimental results and analysis

The chains' configurations were monitored over time and used to determine distributions of the chains' orientation. Figure 2 shows the various configurations observed for the three experimental cases in Fig. 1(b). The dynamics of the chains are dictated by the elastogravitational number which is defined as the ratio between gravitational and elastic forces, $\beta = 4\pi a^3 L^2 \Delta \rho g' N/3\sigma_b$, and the persistence length, $L_p = \sigma_b/k_B T$. Here, a is the average radius of the colloidal particles, L is the contour length, $\Delta \rho$ is the density difference between the colloidal particles and the solvent, g' is the magnitude of the gravitational acceleration projected in the direction of motion, N is the number of beads in the respective chain, σ_b is the bending modulus of the chain, k_B is the Boltzmann constant, and T the temperature. Interchain hydrodynamic interactions are not taken into account in our analysis. Although such effects are known to play a key role in the dynamics of concentrated filaments suspensions [9,30,31], these are not relevant for the system in Fig. 1(a). Not only are the

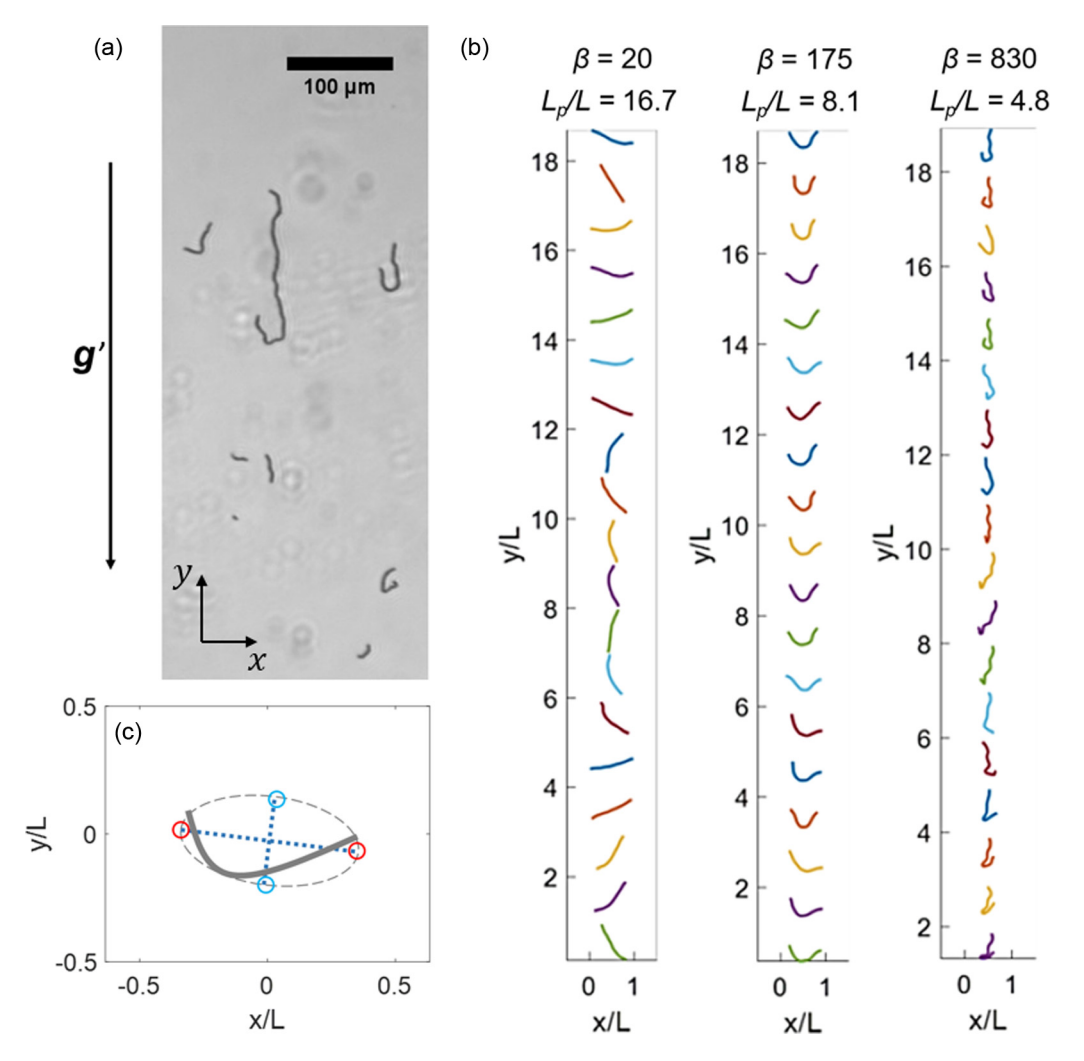


FIG. 1. Visualization of the settling dynamics of semiflexible chains. (a) Snapshot of the chains settling in the chamber with the effective gravity \mathbf{g}' . (b) Tracking the contour evolution of three different chains. From top to bottom, these configurations represent chain sedimentation over a period of 20 minutes, taken at a time interval of 1 min. The contours are normalized by the length of each filament. (c) Schematic drawing of the relationship between a filament and the eigenvectors of its gyration tensor. The ending points of eigenvectors are marked in hollow dots, with the primary vector marked in red and the secondary vector marked in blue.

densities low, but any long-range hydrodynamic interactions will be screened out by the presence of the walls of the chamber [32].

For the case of $\beta=20$, thermal fluctuations were observed throughout the chain contour; however, deflections induced by gravity are not significant. As the chain settles, the thermal motion promotes rotations of the chain, creating an orientation distribution. This orientation distribution swipes all the possible inclinations, i.e., $-\pi/2$ to $\pi/2$, but a weak tendency to stay perpendicular to gravity was evidenced by the increase in the red intensity in such a direction. One should not associate the eventual complete rotations of the chain with tumbling dynamics, given that it is induced by Brownian motion and not hydrodynamic phenomena.

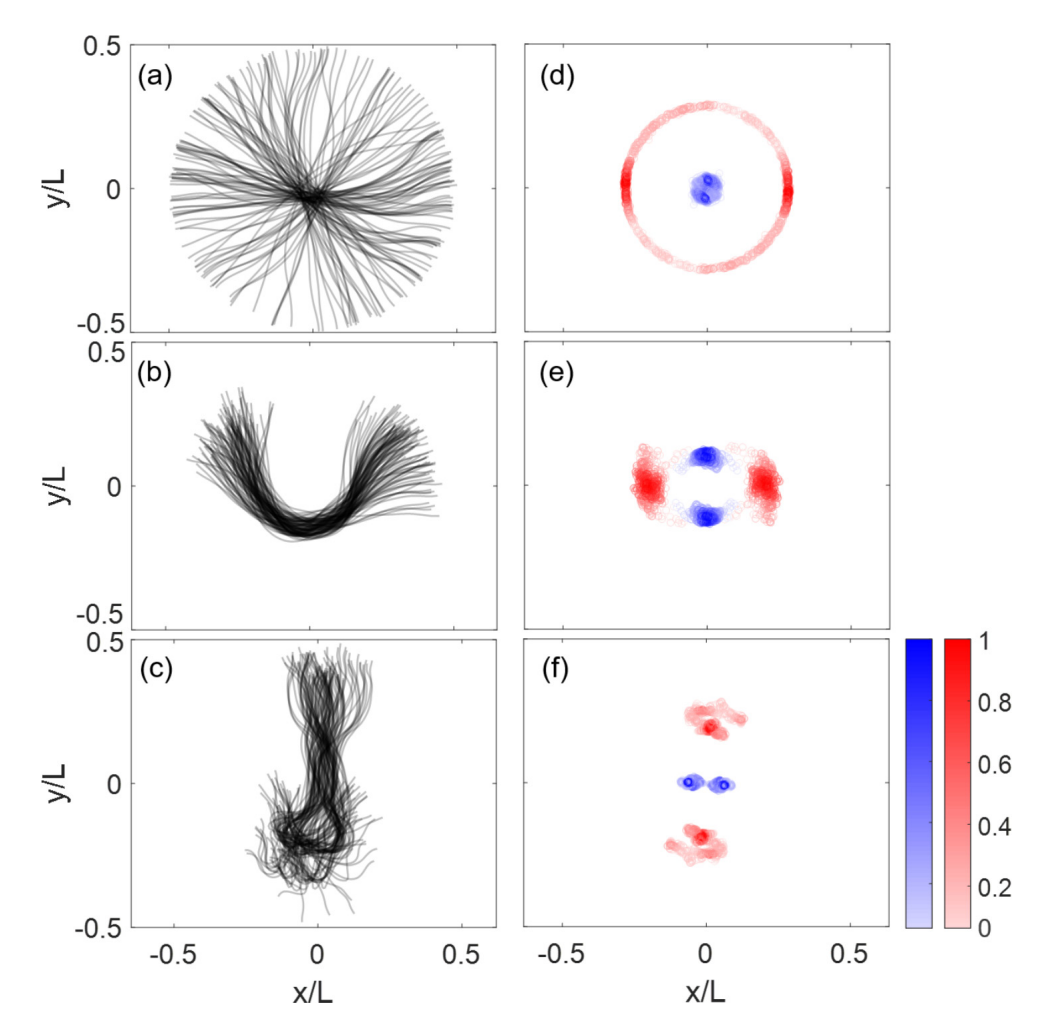


FIG. 2. Configurational and orientational fluctuations during Brownian chains' sedimentation. Superimpositions of the configurations over time of three sediment filaments. They are examples of the three dynamical regimes with $\beta=20,\ 175,\ 830,\$ and $L_p/L=16.7,\ 8.1,\ 4.8,\$ respectively. One hundred snapshots of configurations are plotted out for each case. They were evenly sampled during the 20 min of experimental observation. Shapes were normalized by filament contour length with their center of mass at the origin. Items (e)–(g) are the eigenvector plots of the shapes shown in (a)–(c), respectively. The color bar shows the possibility for the end points to show up in each position during the experimental observation.

For $\beta = 175$, the chain deflection due to gravity is evident, resulting in the U-like shape adopted by the chain. The thermal motion induces fluctuations of both arms of the chain around the equilibrium configuration, but fluctuations of the chain orientation were not as pronounced as in the first case. In this sense, the distribution of the primary axis of the gyration tensor orientation was restricted to directions mostly perpendicular to the gravity. Hence, one does not observe complete rotations.

Lastly, for $\beta = 830$ the flexible chain presented a J-like shape with strong fluctuations along its contour. During the experiment, the shorter arm readily flipped sides, however, due to a limited sedimentation length of the observable domain, we were unable to verify the periodicity of this dynamics. Unlike the two other cases, the primary axis of the gyration tensor is mostly parallel to

the gravity. Also, despite it showing strong fluctuations along its contour, no significant orientation distribution was observed.

It is also important to mention that slight asymmetries with respect to the y-direction are possible in the distribution of the eigenvectors, which may be a result of insufficient configuration samplings due to the limitations related to the observable domain of the system and the fact that the chains are not perfectly homogeneous along their length due to the particles-size distribution and stochastic phenomena in the chains assembly process [21].

III. THEORETICAL MODEL

To model the settling dynamics of the colloidal chains, we used the bead-spring model [3,22] in which the N spherical beads with the same radius a have their centers connected by massless springs of length $l_0 = 3a$. Naturally, the colloidal particles and dsDNA linkers represented the beads and springs, respectively. The suspending phase was assumed to be a Newtonian fluid of viscosity η . In the view of the small size of the chains and the characteristic velocity of sedimentation, we have that the surrounding flow is governed by the Stokes equations and the beads dynamics are free of inertia. Nonlocal hydrodynamic interactions were only taken into account between the beads, ignoring the presence of the DNA. Moreover, interacting colloidal particles follow stochastic Brownian dynamics due to thermal fluctuations in the solvent. Thus, the spatial disposition of the particles was evolved in time using [33,34]

$$\mathbf{X}(t + \Delta t) = \mathbf{X}(t) + \mathbb{M} \cdot \mathbf{F}^{\text{nh}} \Delta t + \nabla \cdot (k_B T \mathbb{M}) \Delta t + \mathbf{\Gamma}(\Delta t),$$

$$\langle \mathbf{\Gamma} \rangle = \mathbf{0}, \text{ and } \langle \mathbf{\Gamma}(\Delta t) \mathbf{\Gamma}(\Delta t) \rangle = 2k_B T \mathbb{M} \Delta t,$$
(1)

where **X** is the particles position vector of dimension 3N, \mathbf{F}^{nh} is the force vector of dimension 3N which accounts for all nonhydrodynamic forces acting on the particles, \mathbb{M} is the mobility matrix of dimension $3N \times 3N$ which couples the dynamic of the particles in the view of hydrodynamic interactions, Δt is the time step used in the numerical simulations, and $\Gamma(\Delta t)$ is a vector of dimension 3N that accounts for the particles displacement due to Brownian motion [35].

The mobility matrix can be constructed by the properly assembly of the 3×3 mobility tensors correlating the dynamics of all possible pairs of particles \mathcal{M}_{mn} , for m, n = 1, 2, 3, ..., N [24,34,35]. In this work, we use the Rotne-Prager-Yamakawa mobility tensor [36,37], given by

$$\mathcal{M}_{\rm mm} = \frac{\mathbf{I}}{6\pi \, \eta a} \tag{2}$$

and, for $m \neq n$,

$$\mathcal{M}_{mn} = \begin{cases} \frac{1}{8\pi\eta} \left[\frac{1}{r} (\mathbf{I} + \hat{\mathbf{r}} \hat{\mathbf{r}}) + \frac{2a^2}{3r^3} (\mathbf{I} - 3\hat{\mathbf{r}} \hat{\mathbf{r}}) \right], & r > 2a, \\ \frac{1}{6\pi\eta a} \left[\left(1 - \frac{9r}{32a} \right) \mathbf{I} + \frac{3r}{32a} \hat{\mathbf{r}} \hat{\mathbf{r}} \right], & r \leqslant 2a, \end{cases}$$
(3)

where \mathbf{r} is the distance vector between the center of the particles m and n, $r = |\mathbf{r}|$, $\hat{\mathbf{r}} = \mathbf{r}/|\mathbf{r}|$, and \mathbf{I} is the identity tensor. Important to mention that, for the chosen mobility tensor, $\nabla \cdot (k_B T \mathbb{M}) = \mathbf{0}$. Moreover, by construction, \mathbb{M} is a positive-definite matrix for all particles' configuration even when particles overlap [24,38]. Therefore, we can compute the thermal fluctuations, obeying the relations in Eq. (1), as

$$\mathbf{\Gamma}(\Delta t) = \sqrt{2k_B T \, \Delta t} \, \mathbb{B} \cdot \mathbf{z}, \quad \mathbb{B} \cdot \mathbb{B} = \mathbb{M}, \tag{4}$$

where \mathbf{z} is a standard normal random vector of dimension 3N. In this work, the product $\mathbb{B} \cdot \mathbf{z}$ is calculated using the methodology introduced by Fixman based on the Chebyshev polynomial expansion [39]. The order of the Chebyshev polynomial is defined using the criteria presented by Jendrejack *et al.* [40–42] considering a relative error of 10^{-3} .

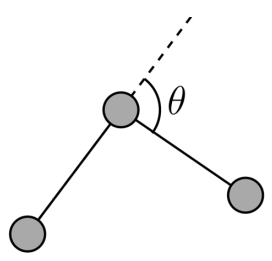


FIG. 3. Definition of the angle θ used for the computation of bending forces.

The gravitational force acting on each particle is taken into account considering the Archimedes' principle

$$\mathbf{f}^g = \frac{4}{3}\pi a^3 \pi \Delta \rho \mathbf{g}',\tag{5}$$

where \mathbf{g}' is the effective gravitational acceleration oriented towards $-\hat{\mathbf{y}}$. The mechanical properties of the dsDNA linkers define the elastic properties of the chains, and, therefore, their rigidity. Considering the stretching and bending energies distributed through the chain respectively defined as

$$U^{s} = \frac{\sigma_{s}}{2l_{0}}(r - l_{0})^{2}$$
 and $U^{b} = \frac{\sigma_{b}}{2l_{0}}(\theta - \theta_{0})^{2}$, (6)

where σ_s and σ_b are the stretching and bending moduli, and θ is defined as shown in Fig. 3. From a Hamiltonian perspective, we calculated the elastic forces acting on each particle as

$$\mathbf{f}^s = -\nabla U^s \quad \text{and} \quad \mathbf{f}^b = -\nabla U^b.$$
 (7)

This very same methodology was vastly used in the literature to study the dynamics of semi-flexible fibers [1,25,43]. More recently Marchetti *et al.* [12] highlighted the good agreement between the dynamics of settling non-Brownian continuum fibers obtained from numerical simulations using the bead-spring model and observed in experiments. The authors also pointed out important geometrical aspects when using the bead-spring model to represent a continuous filament.

In the present mathematical model, we do not consider the hydrodynamic interaction of the colloidal particles with the walls of the chamber, thus, screening effects are not captured. However, to capture the 2-D nature of the settling chain dynamics described in Sec. II, an artificial parabolic potential was introduced in the *z*-direction such that

$$\phi(z) = \frac{4}{3}\pi a^2 \Delta \rho g' \frac{z^2}{2}.\tag{8}$$

Due to the stochastic dynamics of the chains introduced by the thermal forces, it becomes of great importance to consider the steric interactions between the beads to avoid nonphysical configurations and singularities related to the hydrodynamic formulation. To this end, we account for the interaction of two beads as elastic spheres following the well-known Hertz description. The elastic modulus and Poisson's ratio of the particles were empirically chosen to minimize the particles' interpenetration and also avoid numerical instabilities. As soon as these conditions are satisfied, the Hertz forces do not play a significant role in the chain dynamics.

The non-dimensionalization of the problem was done using the chain's contour length L and the Stokes terminal velocity $2a^2\Delta\rho g/9\eta$ as characteristic scales. In this sense, we get that the dynamics of the settling Brownian chains are defined by three dimensionless groups. The first is β , as previously described in Sec. II. Second, the chain's stretching-to-bending ratio $\lambda = \sigma_s L^2/\sigma_b$, which, from the Euler-Bernoulli beam-theory for a circular cross-section becomes $\lambda_E = 4L^2/a^2$ assuming the radius of the cross-section as the particle radius. Throughout this work, we presented the results as a

function of $\lambda^* = \lambda/\lambda_E$. Third, the gravitational Peclet number defined as $Pe_g = 2\pi a^3 \Delta \rho g L/3k_B T$. Note that NPe_g/β equals $L_p/2L$.

A. Non-Brownian chains

Here, we studied the settling dynamics of non-Brownian chains. A better understanding of the chains' dynamics in the absence of thermal motion is needed for further analysis related to the Brownian cases. First, we investigated the steady-state chain configurations as a function of β . Then, we analyzed the dynamics leading the filaments to the metastable W-like shape. Lastly, we focused on the mechanisms of reorientation observed for elastic polymers.

1. Steady-state sedimenting chain configurations

First, we considered a single chain initially straight and perpendicular to gravity. For all cases in this section we set $\lambda^* = 1$. As the chain started to settle, the hydrodynamic interactions lead the center region to fall faster than the ends, causing the chain to bend until it reached a steady-state configuration defined by the balance between drag and elastic forces [5]. It is important to note that these bending dynamics are a consequence of nonlocal hydrodynamic interactions between the beads, otherwise, the chain would settle in a straight configuration [2,3,12].

Figure 4(a) presents the bending amplitude of the chains at the steady-state configuration as a function of β for different N values. The bending amplitude was measured as the indentation δ , normalized by L. The configuration of the chains for the respective values of β and N=31 are indicated by the black arrows. Notably, the curves collapsed as N increased. This behavior suggests that the chain recovers the dynamics of a continuum filament at sufficiently large N. Additionally, Fig. 4(b) illustrates the computed frictional coefficient in the gravity direction normalized by the rigid filament case γ/γ_0 , where $\gamma_0 = \gamma(\beta \to 0)$. The frictional coefficient is simply calculated by the settling velocity of the chain divided by the total gravitational force. Finally, Fig. 4(c) shows the bending energy E^* , normalized by the gravitational potential. As these two physical parameters are dictated by the configuration of the chains, they are also a function of β .

In the limiting case of $\beta \to 0$, chain elasticity dominates over gravitational forces, resulting in a filament settling as a rigid rod perpendicularly oriented to gravity. In this limit, γ is maximum and E^* is the lowest since chain curvature was insignificant. The regime of small deformations occurs for $\beta < 200$ where $2\delta/L \lesssim 0.4$. This regime is characterized by a linear relationship between δ and E^* with β . The chains presented V-like shapes, curved at the center, but with wide open and straightened arms. Due to the small deflections, the chain remained mainly orthogonal relative to gravity and γ/γ_0 is approximately unity.

For $200 < \beta < 800$, chain elasticity and gravitational forces are of similar magnitude. In this regime, the chain configuration transitioned from a V-like to a U-like shape. The $2\delta/L$ plateaus to a saturated value. The curvature increased at the center of the chain, which caused the arms to become parallel to each other. As a consequence, a strong decay of γ/γ_0 is observed, falling from values close to unity to 0.7. Also, E^* peaked at $\beta \approx 350$ due to the larger deflections along the relatively rigid filament.

Lastly, for $\beta > 800$, the resulting chain configuration was dominated by gravitational forces. The U-like shapes slowly transitioned to horseshoe-like shapes, where the ends become closer with β . However, there is no significant variation in $2\delta/L$, which remains approximately 0.85 [12]. This saturated regime also showed small variations of the friction factor $\gamma \sim \beta^{-0.03}$ and a decay in the bending energy of $E^* \sim \beta^{-0.9}$.

Moreover, for $\beta > 3000$, the presence of metastable W-like shapes was observed, represented in Fig. 4 by the solid symbols. These W-like shapes evolved to the stable horseshoe-like shapes after small numerical disturbances — $\mathcal{O}(10^{-16})$ — associated with the precision of the computer. The W-like shapes are characterized by larger values of γ/γ_0 and E^* due to, respectively, the larger chain section perpendicular to gravity, and the creation of two more bending modes. A deeper analysis of this configuration is presented in Sec. III A 2.

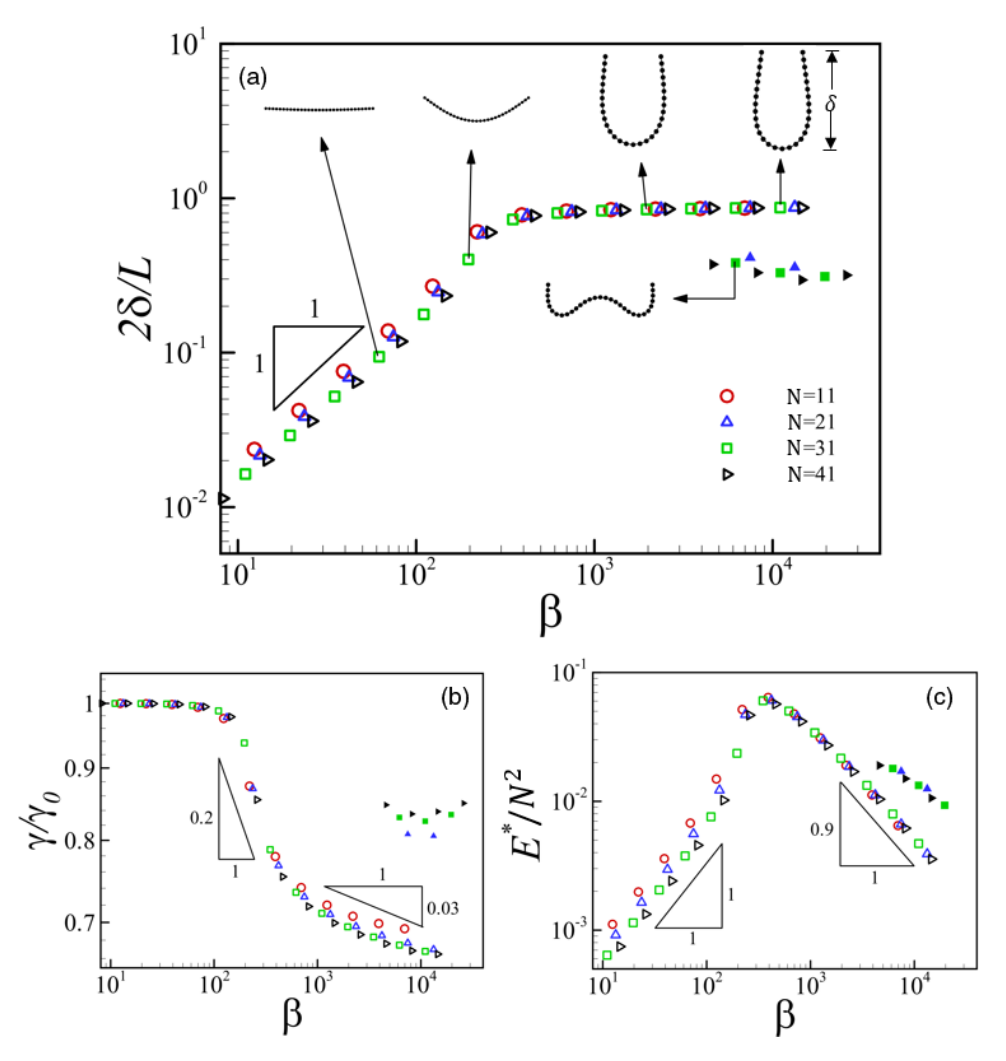


FIG. 4. Chains steady configurations as a function of β for different numbers of beads. (a) Bending amplitude δ . As insets, we have the chains configurations for N=31 at different values of β , as indicated by the arrows. (b) Friction coefficient for motion in the gravity direction γ , normalized by the friction coefficient at the rigid limit γ_0 . (c) Bending energy normalized by the gravitational potential E^* . The solid symbols represent the measurements for the chains at the "W" configuration. All plots are in log-log scale.

2. Metastable W-like chain configurations

The W-like metastable chain configuration has been reported in simulations of the sedimentation of highly flexible fibers, but experimental observations have not been reported [3,9,12]. In this section, we offer a deeper investigation of this phenomenon. Figure 5 presents the shape evolution of three different chains $\lambda^* = 1$, 0.1, and 0.01, for $\beta = 3100$ and N = 31. Although $\lambda^* = 0.01$ is typically difficult to realize, studying such a case helps our understanding of the dynamics that lead the chains to the W-like configuration. Initially, for all the studied λ^* , the nonlocal hydrodynamic interactions induce the beads at the center to fall faster, causing the inclination of both ends while the center remains in the original orientation. In this configuration, due to the difference between the drag coefficients perpendicular to and parallel to the segment's longitudinal axis, the inclined arms at both ends are pushed towards the center while their relative settling speed is increased.

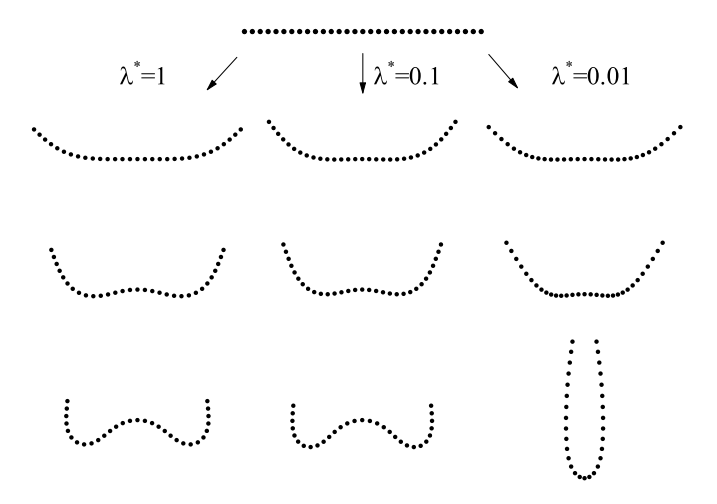


FIG. 5. Evolution of the chain to the W-like configuration for $\lambda^* = 1$, 0.1, and 0.01, setting $\beta = 3100$ and N = 31.

Under such circumstances, the chain is driven to the W-like shape, with the center region being compressed by the lateral motion of the inclined arms. For $\lambda^* = 1$ and 0.1, the filament reached the metastable W-like shape. However, for $\lambda^* = 0.01$, the density of beads per chain length increased in the center as a result of transverse movement of the beads because there is little resistance to compression, which also results in a greater mobility of the segment. The result is that the center of the chain falls faster than the arms; hence, the metastable W-like shape is not observed. From these simulations, the metastable W-like shape arises from dynamics in which a buckling mode in the filament is formed to relieve stresses due to the compression of a region. Experimentally, this shape is rare to be observed given that the dynamics leading to it is highly dependent on the filament initial condition, the high flexibility of the filament, and due to its metastable nature [12]. However, buckling-like dynamics might be induced to chains by means of dipolar interactions [26].

3. Elastogravitational reorientation

The lack of rotation in the sedimentation of individual rigid rods is a well-known phenomenon in the literature. However, when small deflections are present, the filaments rotated to align their end-to-end direction with gravity [2,4,12]. This rotation is due to the asymmetry in the inclination angles between the sides of the chain with respect to gravity. Here, we define the chain inclination θ as the angle between the primary axis of the gyration tensor and the horizontal direction, such that at equilibrium $\theta = 0$. For highly deflected chains, for which the primary axis of the gyration tensor may flip from parallel to perpendicular to the end-to-end direction, θ is defined from the secondary eigenvector of the gyration tensor. Given that the hydrodynamic torque is a consequence of the chain's deflection, it must be dependent on θ . Moreover, as a restorative mechanism, it does also depend on θ . Lastly, in view of the linearity of the Stokes equations, the angular velocity of the chains should follow a linear relationship with the hydrodynamic torque. Following this argument and assuming small deflections, the chain dynamics are governed by $\dot{\theta} = -\theta/\tau^H$, with a characteristic time of hydrodynamic reorientation $\tau^H \sim 1/\theta$. Chain reorientation can be interpreted as a relaxation of the chain inclination driven by a hydrodynamic torque [3].

The results for reorientation dynamics of settling chains initially inclined at $\theta_0 = \pi/4$, for $\lambda^* = 1$ and N = 31 are shown in Fig. 6. The time required Δt for a chain to evolve from θ_0 to $\theta \le 0.0175$, as a function of β is shown in Fig. 6(a). Included in the figure are representations of the chain shape evolution for the respective cases, as indicated by the arrows. Three distinct mechanisms of reorientation based on the flexibility of the chain are observed. To better understand these

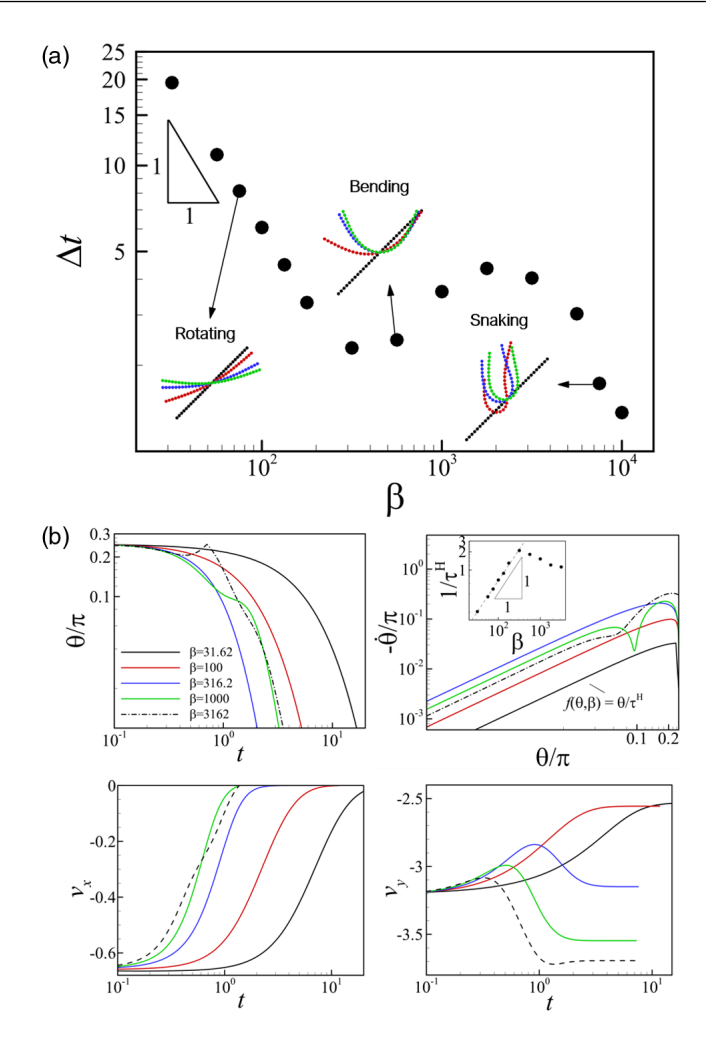


FIG. 6. Reorientation dynamics of settling chains, for N=31 and $\lambda^*=1$. (a) Reorientation time Δt as a function of β . Schematics of the chains' shape evolution for the respective cases are indicated by the arrows. (b) The plot in the top-right presents θ as a function of time. The plot in the top-left presents angular velocity $\dot{\theta}$ as function of the the inclination. The plots in the bottom presents v_x and v_y as a function of time. The cases under consideration are $\beta=31.62$ (solid black line); $\beta=100$ (solid red line); $\beta=316.2$ (solid blue line); $\beta=1000$ (solid green line); $\beta=316.2$ (dashed black line).

mechanisms, Fig. 6(b) plots the chain's reorientation dynamics for key parameters, such as θ , θ , and the velocity of the chain's center of mass parallel to and perpendicular to gravity, v_y and v_x , respectively. For $\beta \lesssim 300$, chain rotation about its center of mass was the dominant mechanism, identified as *rotating*. The curves for $\theta(t)$ presented a monotonic exponential decay behavior, indicating a single mechanism of relaxation. Moreover, from a linear regression $1/\tau^H \approx 0.0059\beta$.

For intermediate values of $300 \lesssim \beta \lesssim 2000$, *quasi*-independent rotation of the two sides of the chain about the center occurs. This is characterized as the *bending* mechanism, which aims to maximize the chain bending for a respective value of β . Chain rotation may occur if the arms are not parallel, or a faster settling velocity of the longer arm when the arms are parallel. One can observe for the case $\beta = 1000$ that the inclination of the chain does not present a monotonic evolution, but, rather, the presence of two mechanisms with different relaxation times, one for $t \lesssim 0.1$ and another for $t \gtrsim 0.1$. As previously mentioned, the first is characterized by the bending of the chain towards

the U-shape, with a rapid decrease of θ . However, this mechanism may lead to slight differences between the lengths of the arms, which is more pronounced with increasing β . Such a unbalance is corrected in the second period, when the largest arm falls faster until symmetry is reached.

For $\beta > 2000$, the sedimenting chains initially form J-like shapes. Here, the chain initially curls, followed by a faster settling velocity of the longer arm until chain symmetry is reached. This *snaking* mechanism has similar dynamics to those observed for semi-flexible filaments in shear flows [44]. For $\beta = 3162$, one can observe the flip of the main axis of the gyration tensor with respect to the end-to-end direction highlighted by the discontinuity of the $\dot{\theta}(t)$ at $t \approx 0.8$. This discontinuity is not shown in the plot of $\dot{\theta}(\theta)$ for convenience. In this regime, the reorientation time decreases with β once the weak elastic forces result in reduced resistance to chain bending. It is important to mention that the transitions between the reorientation dynamics with β are smooth and share mechanisms characteristic of both regimes. Also, for all cases, a regime of exponential decay is reached, as indicated by the linear relation $\dot{\theta} \sim -\theta$.

The chain settling velocity and lateral migration is also investigated by measuring the horizontal and vertical velocities of the chain center of mass, respectively, v_x and v_y , as presented in Fig. 6(b). In the rigid limit, $\beta \to 0$, $v_x \sim (\kappa - 1)\cos\theta\sin\theta$ and $v_y \sim \kappa\sin^2\theta + \cos^2\theta$ [22], where $\kappa = 2[\log(L/2a) + \chi^{\parallel}]/[\log(L/2a) + \chi^{\perp}]$ is the perpendicular-to-parallel friction coefficient ratio. Considering that the hydrodynamic interactions between the particles are governed by the Yamakawa-Rotne-Prager, $\chi^{\perp} = 1.111$ and $\chi^{\parallel} = 0.044$ [45,46]. For $\beta = 31.62$, N = 31, and $\lambda^* = 1, \kappa \approx 1.525$ is measured from the simulations. Despite the small deflections, good agreement with the theoretical value $\kappa \approx 1.566$ is obtained. Note that the negative value of v_x indicates that the chain translates to the left. Regardless of the different mechanisms of reorientation, the curves of v_x present a similar trend. On the other hand, the curves for v_y are strongly influenced by β . Initially, the settling velocities are the same for all cases, given that the initial chain configurations are identical. For stiff chains, v_y decreases as the chain reorients, until it reaches its steady-state configuration. However, for flexible chains, an inflection of v_y is observed as a consequence of the large chain deflection, as discussed in Sec. III A 1. This configuration results in a faster settling velocity for more flexible chains. In fact, the terminal settling velocity for the chains must obey an inverse relation with γ/γ_0 such that it can be obtained from the curve for $\gamma(\beta)$ in Fig. 4.

B. Brownian chains

In this section, Brownian motion is shown to be a determining factor governing the sedimentation of colloidal chains. Thermal fluctuations not only generate local displacements along the chain, measured by the ratio L_p/L , but also can give rise to stochastic chain rotation. In this case, there is a competition between the elastogravitational and Brownian torques on the chain orientation. The first effect works as a restorative mechanism (Sec. III A 3), while the second induces stochasticity in the chain orientation.

The superposition of the chain configurations at distinct times, for different values of β and Pe_g is shown in Fig. 7. For all cases N=31 and $\lambda^*=1$. At small values of $\beta \leq 200$, the competition between the elastogravitational and Brownian torques defines the distribution of the chain orientation. Fluctuations over the contour length are not evident for the respective cases $L_p/L \gtrsim 7.8$ across all values of Pe_g . Since the chains are relatively rigid, thermal fluctuations do not play a significant role on the shape, but promote translation and rotation of the chain. Hence, the chains remain in a slightly bent configuration, characteristic of their corresponding non-Brownian case. For $400 \leq \beta \leq 1600$, the chains present well-defined U-like configurations. As the chain becomes less rigid, the propagation of elastic stress through the chain decreases, and thermal effects are likely to promote local deformation rather than chain translation and rotation. Fluctuations of both arms around the equilibrium configuration may lead to variations of θ , but this is not attributed to chain rotation. As the values of β increases and Pe_g decreases, the shape of the chains becomes amorphous. The shape fluctuations may lead the system to follow complex dynamics, e.g., the snaking reorientation dynamics explored in Sec. III A 3, given the increased degrees of freedom

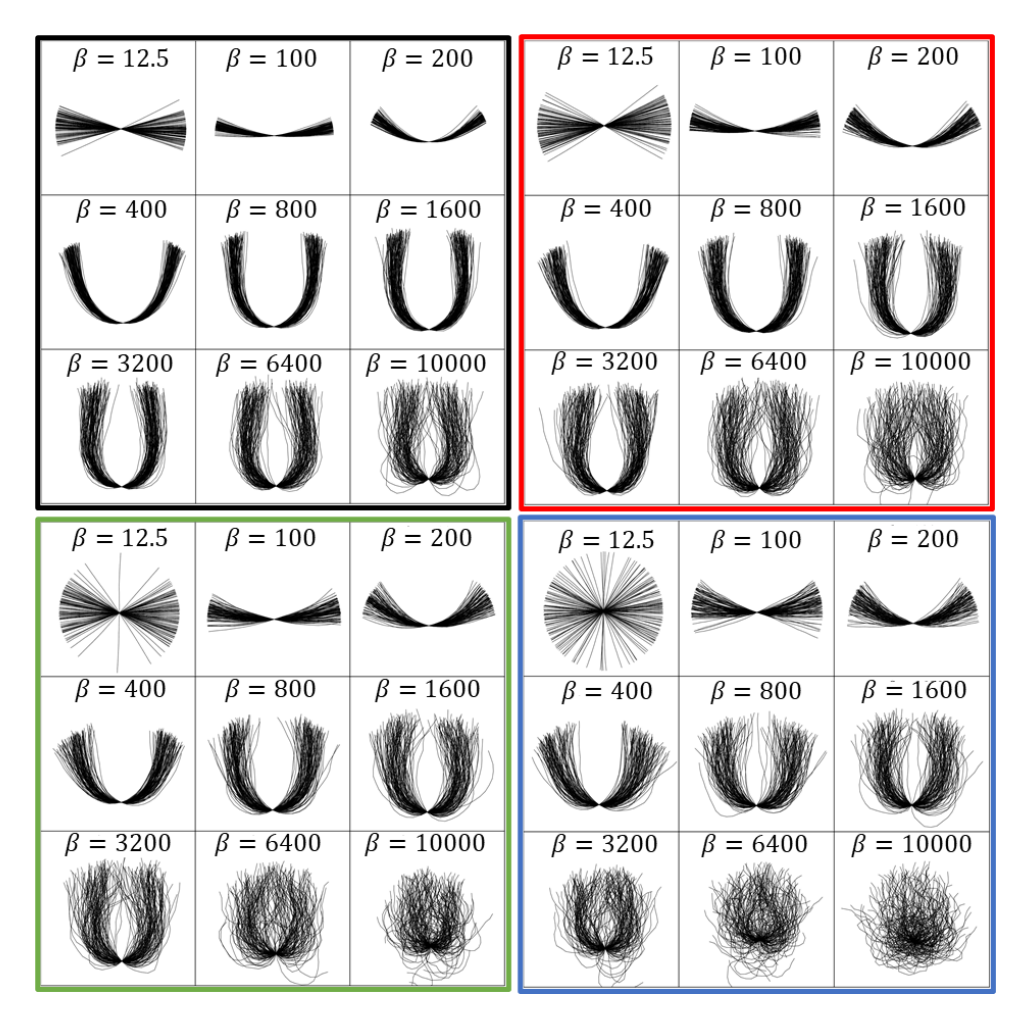


FIG. 7. Configuration of sedimenting Brownian chains projected in the xy plane for various values of β and Pe_g . The cases in the black, red, green, and blue boxes correspond, respectively, to $Pe_g = 200$, 100, 50, and 25. Each simulation corresponds to a non-dimensional period of time equal to 1000. Chain configurations at distinct times are superimposed with respect to the center bead.

coupled with nonlocal hydrodynamic interactions. For the case $\beta = 10\,000$ and $Pe_g = 25$, which corresponds to $L_p/L \approx 0.16$, the U-like chain shapes cannot be easily identified.

Figure 8 provides statistical measurements for the chains inclination, settling velocity, and horizontal displacement. The effect of Pe_g on the chains' inclination distribution during sedimentation is shown in Fig. 8(a). All cases present a Gaussian-like distribution with a zero mean, highlighting the competition between restorative elastogravitational and stochastic thermal fluctuations. Such results are in agreement with the analytical analysis developed by Manikantan *et al.* [30]. For $\beta \leq 200$, the distribution narrows with β ; while for $\beta \geq 800$, the standard deviations are, respectively, large for all cases, and do not present clear dependence on the elastogravitational number. To better elucidate this relationship, Fig. 8(b) shows the standard deviation of the inclination distributions, $\sigma(\theta)$, as a function of β . A clear scaling $\sigma(\theta) \sim \beta^{-0.5}$ is observed over all values of Pe_g when $\beta \leq 200$. This corresponds to the regime in which the thermal fluctuations mainly induce chain translation/rotation, rather than deformation. Also, this is the regime in which we verify that rotation is the dominant mechanism governing the chains' reorientation dynamics, as previously

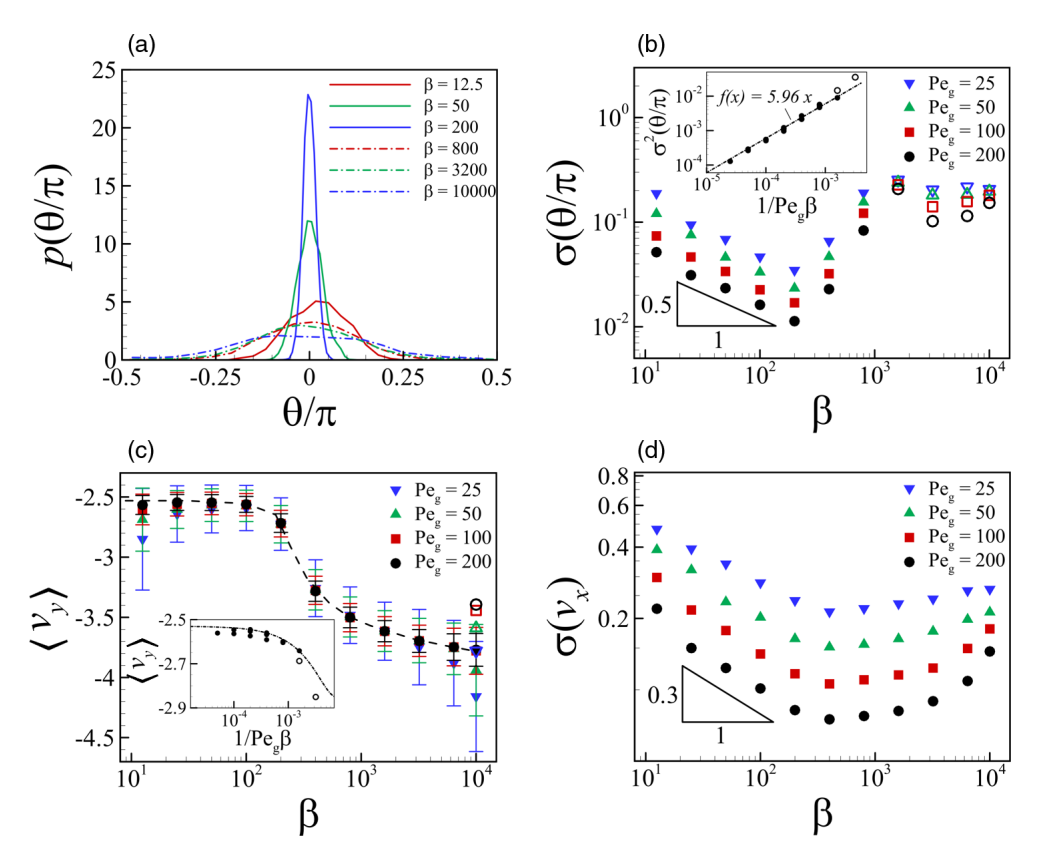


FIG. 8. Brownian chains dynamics during sedimentation. (a) Inclination distribution, $p(\theta)$, for $Pe_g = 100$ and different values of β . (b) Standard deviation for θ as a function of β at different values of Pe_{g} . The open symbols refer to cases in which, at the equilibrium, the primary eigenvector of the gyration tensor relies close to the gravity direction. As the inset, we have the variance of θ as function of $1/Pe_g\beta$ for the cases in which $\beta \le 200$. The open symbols refer to the cases $\beta = 12.5$ and $Pe_g = 25$ and 50. Since complete rotations are observed for such cases (see Fig. 7), these are not taken into account in the linear regression. (c) Mean value of the settling velocity v_y as a function of β with respective standard deviation for the different values of Pe_q . The dashed line corresponds to the settling velocity for the respective non-Brownian cases. The open symbols at $\beta = 10\,000$ correspond to the cases in which the parabolic potential in the z-direction is absent. As the inset, we have the mean settling velocity as a function of $1/Pe_g\beta$ for the cases in which $\beta \le 100$. The cases for $\beta = 200$ were excluded from this analysis given that the bent configuration induces a nonnegligible faster settling velocity compared to the rigid cases. The open symbols refer to the cases $\beta = 12.5$ for $Pe_v = 25$ and 50. The dashed-dotted line correspond to the predictions obtained via Eq. (9). (d) Standard deviation for the chain velocity in the horizontal direction v_x as a function of β , for different values of Pe_g . The velocities v_y and v_x are calculated from the displacement of the chain's center of mass over a time period of 0.1. All simulations for the Brownian cases were run for a computational time period of 1000.

discussed in Sec. III A 3. The linear dynamics characteristic of this regime allows us to define a hydrodynamic reorientation potential as a function of the chain inclination $H \sim \theta^2/2\tau^H$. Therefore, assuming equilibrium, the chain orientation distribution follows $p(\theta) \sim \exp(-\theta^2\tau^B/2\tau^H)$, where $\tau^B \sim Pe_g$ is the characteristic time of Brownian rotation. If $\tau_H \ll \tau_B$, a narrow distribution of θ is observed. However, $\tau_H \gg \tau_B$ leads to a uniform distribution due to the inclination periodicity. From the described relationships, we determine that $\sigma^2(\theta) \sim 1/Pe_g\beta$, which is in accordance with the presented results in Fig. 8(b), as highlighted in the inset. As β increases, more complex mechanisms

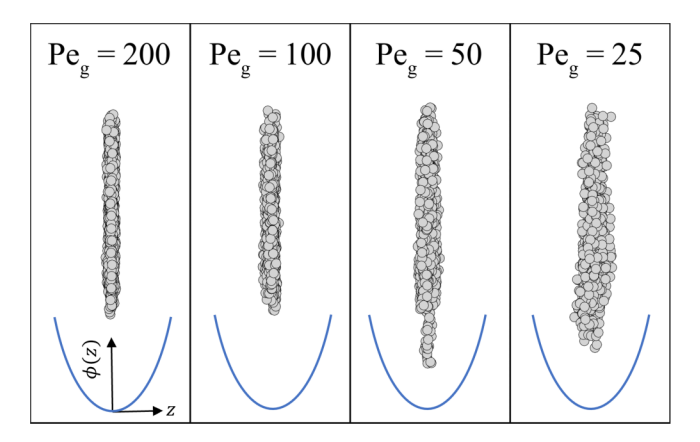


FIG. 9. Configuration of sedimenting Brownian chains projected in the yz-plane for $\beta = 10\,000$ and the different values of Pe_g . The parabolic potential field $\phi(z)$ is represented at the bottom of each case by the blue curve. Differently from Fig. 7, the beads are explicitly shown to elucidate the three-dimensional configuration. Chain configurations at distinct times are superimposed with respect to the center bead.

governing chain reorientation are present; thus, the chains' orientation distribution is no longer a function of $Pe_g\beta$. In fact, a nonmonotonic response of $\sigma(\theta)$ with respect to β and Pe_g is verified. By increasing β from 200 up to 800, $\sigma(\theta)$ rapidly increases while the dependence on Pe_g decreases. At $\beta=1600$, the curves of $\sigma(\theta)$ collapses for all cases of Pe_g . This unexpected result is due to the continuous interchange between the primary and secondary eigenvectors of the gyration tensor as a result of configuration fluctuations, rather than chain inclination. Notably, for $\beta \geqslant 3200$, $\sigma(\theta)$ increases with β , however, with a weaker dependency with decreasing Pe_g . In fact, the curve for $Pe_g=25$ appears to be saturated, suggesting that elastic forces do not plays a significant role on the chains' orientation distribution at high β values.

In addition to changes in the chains' orientation distribution and shape fluctuations, variations in the settling velocity and horizontal diffusion are detected. Figure 8(c) presents the chain settling velocity v_y . For $\beta < 100$ the thermal fluctuations cause the chains to settle faster compared to their respective non-Brownian case, as shown by the dashed curve in Fig. 8(c). Such an effect becomes more pronounced with decreasing Pe_g and β , reflective of the longer time spent in a more inclined configuration, i.e., wider distribution of θ . Combining the above results with the discussion from Sec. III A 3, the theoretical value for the mean settling velocity $\langle v_y \rangle$ of the chain follows

$$\langle v_y \rangle = v_y^0 \int_{-\pi/2}^{\pi/2} (1.525 \sin^2 \theta + \cos^2 \theta) p(\theta) d\theta,$$
 (9)

where the variance in the normal distribution $p(\theta)$ is $\sigma^2 = \psi/Pe_g\beta$, for ψ being computed from the linear regression shown in the inset of Fig. 8(b). The predicted values for $\langle v_y \rangle$ are in great accordance with the values obtained from the simulations for $\beta \leq 100$, as highlighted by the inset of Fig. 8(c). For the cases $Pe_g = 25$ and $Pe_g = 50$ at $\beta = 12.5$, represented by the open symbols, faster settling velocities than the predicted are observed given that the normal distributions $p(\theta)$ do not reflect the complete rotation of chains presented in Fig. 7. At the limit $\tau_B/\tau_H \to 0$, we expect a uniform distribution of θ , and, consequently $\langle v_y \rangle \to 3.17$. For $\beta > 100$, the mean settling velocity converges to the one correspondent to the respective non-Brownian cases. However, an interesting phenomenon is observed for $\beta \gtrsim 1600$ and $Pe_g \leq 50$. In the presence of increasing thermal fluctuations, the high flexibility of the chains leads to configurations in which the beads are no longer confined to the xy-plane z = 0, i.e., beads can be seen side-by-side in the z-direction as shown in Fig. 9. On top of that, the compression caused by the parabolic potential in the z-direction reduces the overall distance between the beads, resulting in a faster average settling

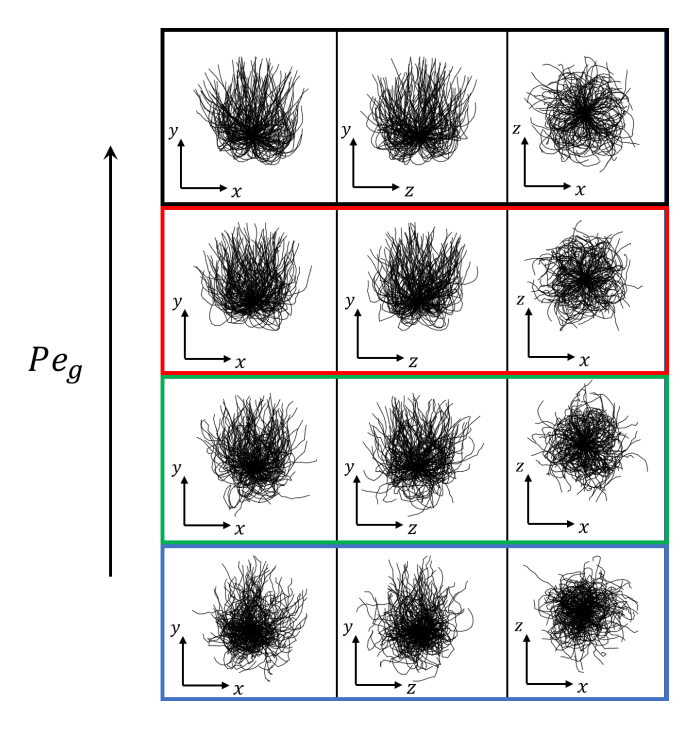


FIG. 10. Configuration of sedimenting Brownian chains in the absence of the parabolic potential, $\phi(z)$, for $\beta = 10\,000$, and $Pe_g = 200$, 100, 50, and 25, from top to the bottom (black, red, green, and blue), respectively. From left to the right, we see the chains projected in the xy, zy, and xz planes, respectively. Chain configurations at distinct times are superimposed with respect to the center bead.

velocity compared to the non-Brownian respective cases. Such an effect becomes more pronounced as β increases and Pe_g decreases.

For a better understanding of this effect, we simulated the cases for $\beta=10\,000$ in the absence of the parabolic potential field, i.e., for chains no longer confined to the xy-plane. We observed that for all cases the settling velocity reduces compared to the respective cases with the parabolic potential. By contrast, we found that the settling velocity is increased for lower values of Pe_g . When the beads are free to spread into the z-direction due to thermal fluctuations, we observe configurations less likely to have beads aligned in the direction of motion. Such an effect increases the average drag on the chains, reducing the average settling velocity, similar to what happens for rigid rods settling perpendicular to their orientation. This behavior is a direct consequence of the long-range hydrodynamic interactions. Thus, thermal fluctuations lead to configurations less hydrodynamically favorable to sedimentation. By contrast, lower values of Pe_g result in more compact configurations of the chains, highlighted by the denser core regions in Fig. 10. These more compact chains experience greater hydrodynamic interactions and faster sedimentation, similar to what is observed for the sedimentation of blobs of particles [47].

Figure 8(d) shows the chain lateral diffusion represented by the standard deviation of the horizontal velocity $\sigma(v_x)$, as a function of β . A similar trend is observed for all values of Pe_g . Initially, for $\beta \le 200$, the chains' lateral diffusion decreases as the orientation distribution narrows, i.e., increasing β and Pe_g . We also found from simulations that in this regime $\sigma(v_x)$ nearly scales with $\beta^{-0.3}$. Despite the fact that $\sigma(\theta)$ increases significantly with β for $200 \le \beta \le 800$, $\sigma(v_x)$ barely responds to variations of β in this regime. In fact, for all cases of Pe_g , $\beta = 400$ presents the smallest horizontal diffusion due to the characteristic U-like chain shape and small inclination variance. For higher values of β and, consequently, more complex configurations, increasing lateral

displacements are observed. It is worth noting that, from the responses observed for v_y and $\sigma(v_x)$, we are able to define statistical trajectories and lateral migration for the settling Brownian chains.

IV. CONCLUDING REMARKS

We present an experimental and computational study aimed at understanding the settling dynamics of Brownian colloidal chains. The experimental system consists of colloidal particles linked together with double-stranded DNA. Brownian motion is shown to play an important role in the orientation dynamics of these filaments. Given their controllable elasticity and contour length, such systems are of great value to study and understand the dynamics of Brownian filaments under a vast range of physical regimes. A bead-spring model is used to simulate the sedimentation of these filaments. We verify that the dynamics of the non-Brownian chains are defined by the elastogravitational number β , which measures the ratio of the gravitational-to-elastic forces. As the value of β increases, the equilibrium shape of the chains transit from linear to U-like shapes. Also, the flexibility of the chains induces three distinct reorientation mechanisms, with different characteristic times, driving the chains to orient with their end-to-end direction perpendicular to gravity.

For the numerical simulations of the Brownian cases, we considered an artificial parabolic potential in the direction perpendicular to gravity to mimic the approximate 2-D nature of the experimental setup. We observed a strong dependence of the chain dynamics on the gravitational Peclet number, Pe_g , which is the ratio of gravitational-to-thermal forces. For rigid filaments, thermal fluctuations promote chain rotation/translation while gravitational-elastic effects cause chain reorientation. This results in a Gaussian-like distribution of the chains' orientations, where the variance is a linear function of $1/Pe_{\rho}\beta$. Nonetheless, the fluctuations of the chains' inclination induce a faster settling velocity when compared with their respective non-Brownian cases. As the chains become more flexible, the thermal fluctuations induce larger shape fluctuations and less chain rotation. For highly flexible chains, the thermal fluctuations result in amorphous chains configurations. Moreover, for the cases in which the thermal fluctuations are strong enough to overcome the confinement promoted by the parabolic potential, the chains presented faster settling velocity which increased for lower values of Pe_g . In the absence of the parabolic potential, i.e., the fully three-dimensional case, and at highly flexible regimes, reducing Pe_g also showed to increase the settling velocity. It is clear that Brownian forces play an important role in the sedimentation of colloidal filaments. The chain flexibility provides additional degrees of freedom that give rise to new and complex dynamics.

ACKNOWLEDGMENT

This work was funded by the National Science Foundation (NSF) under Grants No. CBET-17055703, No. DMR-1826623, and No. PHY-2019745.

^[1] O. Du Roure, A. Lindner, E. N. Nazockdast, and M. J. Shelley, Dynamics of flexible fibers in viscous flows and fluids, Annu. Rev. Fluid Mech. 51, 539 (2019).

^[2] X. Xu and A. Nadim, Deformation and orientation of an elastic slender body sedimenting in a viscous liquid, Phys. Fluids 6, 2889 (1994).

^[3] M. C. Lagomarsino, I. Pagonabarraga, and C. P. Lowe, Hydrodynamic Induced Deformation and Orientation of a Microscopic Elastic Filament, Phys. Rev. Lett. **94**, 148104 (2005).

^[4] X. Schlagberger and R. Netz, Orientation of elastic rods in homogeneous stokes flow, Europhys. Lett. 70, 129 (2005).

^[5] L. Li, H. Manikantan, D. Saintillan, and S. E. Spagnolie, The sedimentation of flexible filaments, J. Fluid Mech. 735, 705 (2013).

- [6] S. Jung, S. E. Spagnolie, K. Parikh, M. Shelley, and A.-K. Tornberg, Periodic sedimentation in a stokesian fluid, Phys. Rev. E 74, 035302(R) (2006).
- [7] M. Bukowicki and M. L. Ekiel-Jeżewska, Different bending models predict different dynamics of sedimenting elastic trumbbells, Soft Matter 14, 5786 (2018).
- [8] I. Llopis, I. Pagonabarraga, M. Cosentino Lagomarsino, and C. P. Lowe, Sedimentation of pairs of hydrodynamically interacting semiflexible filaments, Phys. Rev. E 76, 061901 (2007).
- [9] G. Saggiorato, J. Elgeti, R. G. Winkler, and G. Gompper, Conformations, hydrodynamic interactions, and instabilities of sedimenting semiflexible filaments, Soft Matter 11, 7337 (2015).
- [10] M. Bukowicki and M. L. Ekiel-Jeżewska, Sedimenting pairs of elastic microfilaments, Soft Matter 15, 9405 (2019).
- [11] K. Gustavsson and A.-K. Tornberg, Gravity induced sedimentation of slender fibers, Phys. Fluids 21, 123301 (2009).
- [12] B. Marchetti, V. Raspa, A. Lindner, O. du Roure, L. Bergougnoux, E. Guazzelli, and C. Duprat, Deformation of a flexible fiber settling in a quiescent viscous fluid, Phys. Rev. Fluids 3, 104102 (2018).
- [13] E. Duguet, A. Désert, A. Perro, and S. Ravaine, Design and elaboration of colloidal molecules: An overview, Chem. Soc. Rev. 40, 941 (2011).
- [14] Y. Wang, Y. Wang, D. R. Breed, V. N. Manoharan, L. Feng, A. D. Hollingsworth, M. Weck, and D. J. Pine, Colloids with valence and specific directional bonding, Nature (London) **491**, 51 (2012).
- [15] C. E. Snyder, M. Ong, and D. Velegol, In-solution assembly of colloidal water, Soft Matter 5, 1263 (2009).
- [16] L. J. Hill and J. Pyun, Colloidal polymers via dipolar assembly of magnetic nanoparticle monomers, ACS Appl. Mater. Interfaces **6**, 6022 (2014).
- [17] K. Nakata, Y. Hu, O. Uzun, O. Bakr, and F. Stellacci, Chains of superparamagnetic nanoparticles, Adv. Mater. 20, 4294 (2008).
- [18] Z. Nie, D. Fava, E. Kumacheva, S. Zou, G. C. Walker, and M. Rubinstein, Self-assembly of metal-polymer analogues of amphiphilic triblock copolymers, Nat. Mater. 6, 609 (2007).
- [19] A. Spatafora-Salazar, D. Lobmeyer, L. H. P. da Cunha, K. Joshi, and S. L. Biswal, Hierarchical assemblies of superparamagnetic colloids in time-varying magnetic fields, Soft Matter 17, 1120 (2021).
- [20] D. Li, S. Banon, and S. L. Biswal, Bending dynamics of dna-linked colloidal particle chains, Soft Matter 6, 4197 (2010).
- [21] J. Byrom, P. Han, M. Savory, and S. L. Biswal, Directing assembly of dna-coated colloids with magnetic fields to generate rigid, semiflexible, and flexible chains, Langmuir 30, 9045 (2014).
- [22] M. Doi and S. F. Edwards, *The Theory of Polymer Dynamics* (Oxford University Press, Oxford, 1988), Vol. 73.
- [23] P. Szymczak and M. Cieplak, Hydrodynamic effects in proteins, J. Phys.: Condens. Matter 23, 033102 (2010).
- [24] E. Wajnryb, K. A. Mizerski, P. J. Zuk, and P. Szymczak, Generalization of the rotne-prager-yamakawa mobility and shear disturbance tensors, J. Fluid Mech. 731 (2013).
- [25] S. Kuei, B. Garza, and S. L. Biswal, From strings to coils: Rotational dynamics of dna-linked colloidal chains, Phys. Rev. Fluids **2**, 104102 (2017).
- [26] J. Zhao, D. Du, and S. L. Biswal, Nonlinear multimode buckling dynamics examined with semiflexible paramagnetic filaments, Phys. Rev. E 98, 012602 (2018).
- [27] H. Li, T. Shen, D. Vavylonis, and X. Huang, Actin filament tracking based on particle filters and stretching open active contour models, *International Conference on Medical Image Computing and Computer-Assisted Intervention (MICCAI 2009)*, edited by G.-Z. Yang, D. Hawkes, D. Rueckert, A. Noble, and C. Taylor, Vol. 12, Lecture Notes in Computer Science (Springer, Berlin, Heidelberg, 2009), pp. 673–681.
- [28] H. Li, T. Shen, M. B. Smith, I. Fujiwara, D. Vavylonis, and X. Huang, Automated actin filament segmentation, tracking and tip elongation measurements based on open active contour models, Proc. IEEE Int. Symp. Biomed. Imaging 2009, 1302 (2009).
- [29] J. Schindelin, I. Arganda-Carreras, E. Frise, V. Kaynig, M. Longair, T. Pietzsch, S. Preibisch, C. Rueden, S. Saalfeld, B. Schmid, J.-Y. Tinevez, D. J. White, V. Hartenstein, K. Eliceiri, P. Tomancak, and A. Cardona, Fiji: an open-source platform for biological-image analysis, Nat. Methods 9, 676 (2012).

- [30] H. Manikantan, L. Li, S. E. Spagnolie, and D. Saintillan, The instability of a sedimenting suspension of weakly flexible fibres, J. Fluid Mech. 756, 935 (2014).
- [31] E. Nazockdast, A. Rahimian, D. Zorin, and M. Shelley, A fast platform for simulating semi-flexible fiber suspensions applied to cell mechanics, J. Comput. Phys. 329, 173 (2017).
- [32] Y. von Hansen, M. Hinczewski, and R. R. Netz, Hydrodynamic screening near planar boundaries: Effects on semiflexible polymer dynamics, J. Chem. Phys. 134, 06B609 (2011).
- [33] D. L. Ermak and J. A. McCammon, Brownian dynamics with hydrodynamic interactions, J. Chem. Phys. **69**, 1352 (1978).
- [34] J. F. Brady and G. Bossis, Stokesian dynamics, Annu. Rev. Fluid Mech. 20, 111 (1988).
- [35] J. F. Brady, Brownian motion, hydrodynamics, and the osmotic pressure, J. Chem. Phys. 98, 3335 (1993).
- [36] J. Rotne and S. Prager, Variational treatment of hydrodynamic interaction in polymers, J. Chem. Phys. **50**, 4831 (1969).
- [37] H. Yamakawa, Transport properties of polymer chains in dilute solution: hydrodynamic interaction, J. Chem. Phys. 53, 436 (1970).
- [38] T. Ando, E. Chow, Y. Saad, and J. Skolnick, Krylov subspace methods for computing hydrodynamic interactions in brownian dynamics simulations, J. Chem. Phys. 137, 064106 (2012).
- [39] M. Fixman, Construction of langevin forces in the simulation of hydrodynamic interaction, Macromolecules 19, 1204 (1986).
- [40] R. M. Jendrejack, M. D. Graham, and J. J. de Pablo, Hydrodynamic interactions in long chain polymers: Application of the chebyshev polynomial approximation in stochastic simulations, J. Chem. Phys. 113, 2894 (2000).
- [41] R. R. Schmidt, J. G. H. Cifre, and J. G. de la Torre, Comparison of brownian dynamics algorithms with hydrodynamic interaction, J. Chem. Phys. 135, 084116 (2011).
- [42] T. Geyer and U. Winter, An $\mathcal{O}(N^2)$ approximation for hydrodynamic interactions in brownian dynamics simulations, J. Chem. Phys. **130**, 114905 (2009).
- [43] B. Delmotte, E. Climent, and F. Plouraboué, A general formulation of bead models applied to flexible fibers and active filaments at low reynolds number, J. Comput. Phys. **286**, 14 (2015).
- [44] O. Forgacs and S. Mason, Particle motions in sheared suspensions: X. orbits of flexible threadlike particles, J. Colloid Sci. 14, 473 (1959).
- [45] H. Yamakawa and J.-I. Yamaki, Translational diffusion coefficients of plane-polygonal polymers: Application of the modified oseen tensor, J. Chem. Phys. **57**, 1542 (1972).
- [46] K. Yang, C. Lu, X. Zhao, and R. Kawamura, From bead to rod: Comparison of theories by measuring translational drag coefficients of micron-sized magnetic bead-chains in stokes flow, PLoS One 12, e0188015 (2017).
- [47] G. C. Abade and F. R. Cunha, Computer simulation of particle aggregates during sedimentation, Comput. Methods Appl. Mech. Eng. **196**, 4597 (2007).